Stochastic Model for Quasi-One-Dimensional Transitional Turbulence with Streamwise Shear Interactions

Xueying Wang[1], Hong-Yan Shih[2], and Nigel Goldenfeld[1,3]

[1]*Department of Physics, University of Illinois at Urbana-Champaign, Loomis Laboratory of Physics, 1110 West Green Street, Urbana, Illinois 61801-3080, USA*
[2]*Institute of Physics, Academia Sinica, Taipei 11529, Taiwan*
[3]*Department of Physics, University of California, San Diego, 9500 Gilman Drive, La Jolla, California 92093, USA*

The transition to turbulence in wall-bounded shear flows is typically subcritical, with a poorly understood interplay between spatial fluctuations, pattern formation, and stochasticity near the critical Reynolds number. Here, we present a spatially extended stochastic minimal model for the energy budget in transitional pipe flow, which successfully recapitulates the way localized patches of turbulence (puffs) decay, split, and grow, respectively, as the Reynolds number increases through the laminar-turbulent transition. Our approach takes into account the flow geometry, as we demonstrate by extending the model to quasi-one-dimensional Taylor-Couette flow, reproducing the observed directed percolation pattern of turbulent patches in space and time.

Several important classes of flow, such as Keplerian accretion disks in astrophysics [1] and wall-bounded turbulent shear flows [2], become turbulent through a subcritical transition. In such systems, turbulent structures coexist with laminar flow and exhibit highly nonlinear and complex features. In pipe flow, for example, following a "finite-amplitude" perturbation, transient turbulent local patches, known as "puffs," arise [3] and subsequently decay, split, [4], or grow (in which case they are known as "slugs") [5], depending on the Reynolds number, $\mathrm{Re} \equiv UD/\nu$. Here U is the characteristic flow speed (such as the mean cross-sectional average of the flow speed in a pipe), D is the characteristic length of the system (such as the diameter of a pipe), and ν is the kinematic viscosity of the fluid. The slug regime contains two phases, sometimes termed weak and strong slugs [5]. In the weak slug regime, there is one upstream sharp laminar-turbulent front and no downstream sharp front. In the strong slug regime, there are two sharp fronts, one upstream and one downstream.

Experiments and direct numerical simulations (DNSs) have shown that, near the laminar-turbulent transition in a quasi-one-dimensional (quasi-1D) Taylor-Couette flow, the fraction of turbulence in the system scales with a power law of the deviation of Re from its critical value Re_c, with scaling exponents consistent with a nonequilibrium transition in the universality class of directed percolation (DP) [6], as anticipated by theory [2,7–14]. DP describes the stochastic evolution of active states that coexist with the absorbing state. In terms of transitional turbulence, the local patches of turbulence are an active state, while the laminar state is the absorbing state. Below the critical point,

$\mathrm{Re} < \mathrm{Re}_c$, turbulence decays at long time, while above the critical point $\mathrm{Re} > \mathrm{Re}_c$, turbulence can not only be sustained, but also expands and takes over a portion of the system. At the critical point $\mathrm{Re} = \mathrm{Re}_c$ turbulence can just be sustained, and critical behavior is observed.

Away from the critical regime, the strong nonlinearity of the Navier-Stokes equations has led researchers to propose closure and low-order models to try and capture the emergent features of the flow, including the self-sustaining process [15] and exact coherent structures [16–19]. Near the transition region itself, simulations of a single isolated puff on scales of up to 20 pipe diameters reveal that small-scale turbulence generates an emergent weak large-scale flow that through shear suppresses the turbulence that created it, an activator-inhibitor (or predator-prey) interaction [9,20]. On larger scales, a mean-field model that includes streamwise interactions, based on an analogy of subcritical transitional flows with excitable media, captures much of the flow phenomenology described above [5,8,21–23]. However, none of these approaches provide a complete explanation of the mechanism of puff splitting, puff-puff interactions (pushing), and the puff-slug transition [5,23], nor can they unify the transitional phenomena observed in different flow geometries, such as pipe or quasi-1D Taylor-Couette flow [6].

The purpose of this Letter is to show that the rich phenomenology of quasi-one-dimensional transitional flow can be mimicked (or recapitulated) by a minimal stochastic spatially extended model of the energy budget [24]. We develop a stochastic model for the energy budget and show that it accounts for the full range of transitional phenomena,

including puff decay, splitting, and pushing, as well as the existence and growth of weak and strong slugs. We show that the puff, puff-splitting, and pushing and weak slug regimes are strongly influenced by stochastic effects arising from the limited energy budget available at low Reynolds numbers and is not captured by a leading-order mean-field limit of the governing equations. The strong slug regime occurs at higher Reynolds numbers when the available energy budget is sufficient to drive two fronts. We emphasize the flexibility of our modeling approach in other geometries. For example, it correctly recapitulates the main differences between transitional pipe and quasi-1D Taylor-Couette flows by changing the boundary conditions associated with the mechanism of energy input [6].

Energy budget in pipe and quasi-1D Taylor-Couette flows.—DNS of the Navier-Stokes equations in transitional pipe flow [24] reveals in spatially resolved detail how turbulent energy production mainly arises from the extraction of kinetic energy from the mean flow by large eddies and is balanced by local energy dissipation. This is depicted in Fig. 1(a): large eddies (pictured by the red swirls) extract laminar energy and cause the mean flow speed (spatial profile represented by the blue arrows and energy level by the mean flow energy figure) to decrease. The mean velocity profile (blue curve) becomes blunt compared to the laminar Hagen-Poiseuille flow. The recovery of mean flow kinetic energy as driven by pressure is slower than the extraction of energy by eddies. The difference in timescales results in an energy depletion zone [as indicated in Fig. 1(a)] downstream of turbulent patches where laminar energy is recovered.

Minor differences in energy balance due to the boundary conditions imposed in various geometries can cause qualitative differences in phenomenology. For instance, as depicted in Fig. 1(b), the uniform recovery of mean flow
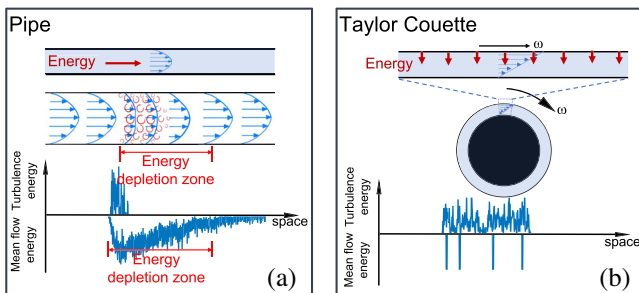

FIG. 1. Schematic of energy profile in (a) pipe flow and (b) Taylor-Couette flow with rotating outer boundary, as studied in [6]. The top figure of (b) shows the enlargement of the thin layer between concentric cylinders shown below. The turbulence energy and mean flow energy snapshot figures are given by the stochastic model. Because of the difference in boundary conditions and energy input, the energy depletion zone (previously termed "refractory region" in [22,23]) is present in pipe flow but absent from the quasi-1D Taylor-Couette flow.

kinetic energy as driven by shearing of the rotating boundary in quasi-1D Taylor-Couette flow is responsible for the lack of energy depletion zone. Such seemingly slight differences induce significant changes in the dynamics of turbulent patches. Our modeling strategy well describes such changes and applies to both geometries equally well.

Stochastic model of the energy transfer process.—Simulations of a single puff in both 10- and 20-diameter-long pipes showed that small-scale turbulence activates a large-scale azimuthal flow structure (zonal flow), which in turn inhibits the turbulence by isotropizing the Reynolds stress [9,20]. This activator-inhibitor relationship resembles that between prey (the activator) and predator (the inhibitor) in a simple ecosystem [25]. That turbulence could excite predator-prey oscillations was predicted nearly 30 years ago [26] and subsequently observed [27] near the low-to-high mode transition in tokamaks.

Note that the predator-prey (or activator-inhibitor) formalism could also potentially apply to other processes that are operative in transitional flows, such as the self-sustaining process [15]. There, vortex rolls give rise to (i.e., activate) streaks, and the energy of the rolls is partly lost to the streak (i.e., inhibited).

These single-puff processes need to be supplemented by the streamwise flow in order to handle puff interactions and provide a complete description of the energy budget including the depletion zone. Let A_i represent a predator (energy of the inhibitory mode) at position i on a spatial lattice, B_j represent a prey (turbulence energy) at position j, and N_k represent nutrient (laminar baseline energy) at position k. The model is formally two dimensional, but is effectively one dimensional because the width of the pipe is much smaller than the length, so that it is a good approximation to average over the width of the pipe. Neighboring individuals are denoted by $\langle ij \rangle$ and all reactions take place only between neighbors, in all four directions with the same probability. In stochastic spatial ecological models such as this, the number fluctuations are controlled by the parameter V that represents the correlation volume of the system [28].

Energy is extracted from the laminar baseline flow (N) and transferred to turbulence (B), represented by $B_i + N_j \xrightarrow[\langle ij \rangle]{b/V} B_i + B_j$. Turbulent energy ($B$) can be transferred to the inhibitory mode (A) through the reaction $A_i + B_j \xrightarrow[\langle ij \rangle]{p/V} A_i + A_j$. This reaction reflects the activator-inhibitor relation between B and A. In addition, the interaction by which A is generated through a mutation of B is allowed by symmetry and so cannot be excluded *a priori*. Thus, we include $B_i \xrightarrow{m} A_i$. These two reactions were already present in the single-puff model [9] that led to the DP universality class [29] for the laminar-turbulent transition. Dissipation of turbulence (B) and zonal flow
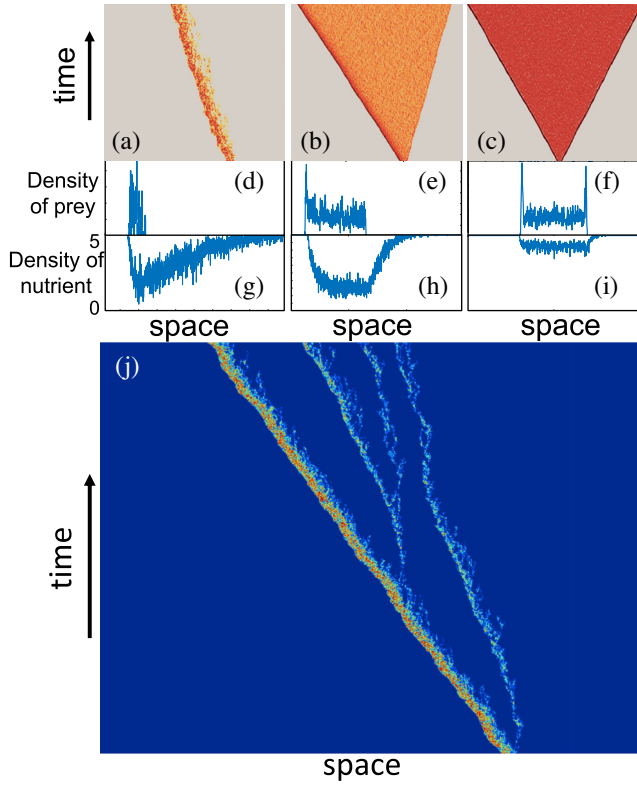
FIG. 2. Monte Carlo simulation of the predator-prey model for transitional pipe turbulence as a function of U (i.e., Reynolds number), showing space (horizontal axis)-time (vertical axis) trajectories of (a) puffs ($U = 0.0165$), (b) weak ($U = 0.1125$) and (c) strong ($U = 0.525$) slugs, and (j) puff splitting ($U = 0.01725$). Simulations used a 2D lattice of size 20×3000 for $30\,000$ time steps (a)–(c) and $100\,000$ time steps (j). Turbulence (prey) profile within puffs and slugs is shown in (d)–(f), mean flow (nutrient) is shown in (g)–(i).

energy (A) is described by the reactions $A_i \xrightarrow{d_A} \phi$ and $B_i \xrightarrow{d_B} \phi$, where ϕ represents the null state in the population model, corresponding to the laminar state of the fluid. There are also two diffusion reactions that describe the spreading of A and B. $A_i \xrightarrow[\langle ij \rangle]{D_A} A_j$ and $B_i \xrightarrow[\langle ij \rangle]{D_B} B_j$.

We include the deterministic advection of mean flow (N) by the reaction $N_i \xrightarrow[\text{prob}=1]{\text{speed}=U} N_{i+1}$. This is implemented at the end of a time step, when all the N's hop forward for one lattice spacing. The advection speed U is realized by rescaling all the other reaction rates and time by $1/U$. With this rule, puffs form in the frame of the simulation, but this is not the laboratory frame. Because of the predation reaction $B_i + N_j \xrightarrow[\langle ij \rangle]{b/V} B_i + B_j$, nutrient effectively attracts prey [29], causing prey patches to drift upstream as shown in Fig. 2. Such drifting is emergent and is observed not just in our ecological model but in numerical simulations of turbulence [30].

Finally, the recovery of the mean flow energy is given by a growth reaction $\phi \xrightarrow{g} N_i$. The reaction rate g is the only nonconstant rate in the model and scales as $g \propto U^2$, reflecting the fact that the laminar solution in pipe flow grows with rate $\propto U^2$ in actual pipe until the steady state Hagen-Poiseuille flow is formed (see Supplemental Material [31] for details).

There is a capacity constraint on the N field mimicking the upper bound on mean flow energy density in the actual system, corresponding to that of the steady laminar Hagen-Poiseuille flow. The hard constraint on site capacity for A and B is represented in the ecological model as a soft constraint (in the conventional way, see, e.g., [32,33]) by two competition reactions $2A_i \xrightarrow{c_A/V} A_i$ and $2B_i \xrightarrow{c_B/V} B_i$ that enforce the logistic growth and saturation of A and B. We set N at the left boundary of the pipe to be the maximum capacity, representing the maximum saturated Hagen-Poiseuille mean flow upstream of turbulence. The system has periodic boundary conditions on the width of the pipe, while the boundaries on the pipe length axis do not matter since the system is large enough that the reactants do not touch the boundaries.

Phase diagram.—We simulate the individual-level predator-prey (PP) model on a two-dimensional lattice of size 20×3000 using a Monte Carlo algorithm, described in detail in the Supplemental Material [31].

Figures 2(a)–2(c) and 2(j) are typical space-time plots of the intensity of B given by the PP model averaged over the width of the pipe. The horizontal axis of the figures is the distance along the pipe, and the vertical axis is time. For each of the figures, we initially perturb the system by randomly generating prey (B) and predator (A) in a small area of size 20×30 in the middle of the lattice, and let the system evolve to form a puff or slug. Figures 2(d)–2(f) are, respectively, snapshot figures of a puff, weak slug, and strong slug of the PP solution, with the vertical axis being the density of prey, representing the turbulent intensity. Likewise, Figs. 2(g)–2(i) are the corresponding snapshots of the nutrient level of the puff, weak slug, and strong slug in Figs. 2(d)–2(f). The figures of puffs and slugs generated by the model closely resemble those seen in DNSs [4,5].

The front speed as a function of U measured from the space-time plots is shown in the main plot of Fig. 3 and is qualitatively comparable to the experimental figure in [5]. The characteristic asymmetry of down- and upstream front speeds in the puff and slug regimes is well captured.

Energy balance and the strong-weak slug transition given by the model.—How does the PP model capture the weak-strong slug transition as U increases? The size of the energy depletion zone in the PP solution is controlled by the nutrient growth rate $g \propto U^2$. The larger U is, the less constraint on prey production is placed by nutrient level, as shown in Figs. 2(g)–2(i). Specifically, when g is large enough, prey production exceeds dissipation, which results in an expanding prey cluster, the slug. The discreteness of
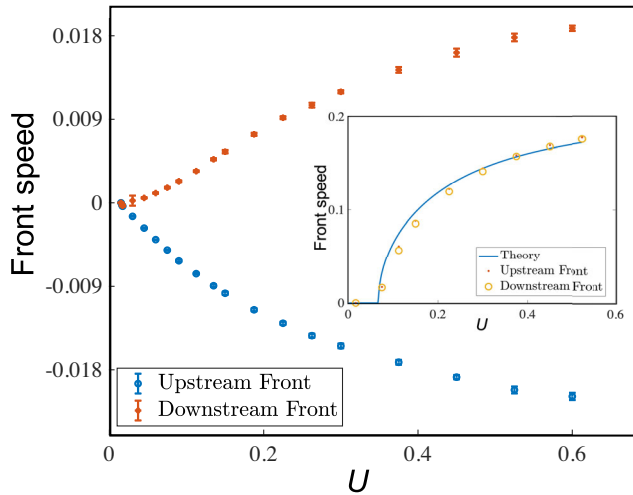
FIG. 3. Mean speed of the upstream front (blue dots) and downstream front (red dots), as functions of U, computed from ten realizations of the Monte Carlo simulation of the stochastic model. Error bars show the standard error of the mean speed and are in some cases not visible. The inset shows absolute value of the deterministic speed of the upstream front (red dots) and the downstream front (orange circles) as a function of speed U calculated from the mean-field limit of the model [31]. The theory curve shown in the inset was calculated using marginal stability analysis [34] described in detail elsewhere [35].

our underlying description is also essential to properly capture the correct phase diagram, because nutrient is absorbed by the prey in quanta. At low U the upstream front absorbs all the incoming quanta, and there are not enough to support a downstream front, leading to a weak slug. At higher U, some quanta pass unabsorbed through the upstream front, enough that a downstream front can be supported; this results in a strong slug with two sharp fronts, one upstream and one downstream. The existence of asymmetric fronts in the weak slug phase are not captured by the leading-order mean-field approximation of the stochastic model—one needs the next order term in $1/\sqrt{V}$ that accounts for the underlying discreteness (see Supplemental Material [31] for derivation). As shown in the inset of Fig. 3, the up- and downstream fronts given by the deterministic theory are entirely symmetric. The detailed mathematical description of these fronts is presented elsewhere [35], but we announce the result here: the mean-field theory for the individual-level model shows that the fronts are related to the well-known Kolmogorov-Petrovsky-Piskunov-Fisher waves [36,37] and are related to the bistable fronts arising in the excitable media models [23] through structural stability [38]. The discreteness in our formulation ultimately corresponds to the subcritical nature of the transition, which implies that transitions between different states are controlled by nonlinear spatially localized modes akin to nucleation phenomena,

leading to superexponential scaling of the timescales associated with puff dynamics [39].

Mechanism for puff splitting.—In the puff phase, nutrient recovers much slower than in slug phases. Nevertheless, when the energy production rate only just exceeds the dissipation rate, a prey cluster can expand. However, it does not form a slug, because when the expanding cluster of prey reaches the energy depletion zone, which is larger with lower U due to the slow nutrient recovery rate, they are more likely to decay. Prey that survives this high decay probability and reaches the end of the energy recovery zone have access to recovered nutrient again and can be locally sustained. When viewed kinematically, the above process appears as if the upstream puff pushes the "daughter" puff away. Note that the entire puff-splitting and pushing process as given by the PP model is stochastic. The low energy influx and stochasticity are the two fundamental ingredients of puff splitting in the model.

With the increase of U, the energy depletion zone becomes smaller, and hence the puff splits more frequently. No clear boundary between puff and weak slug regimes is observed: when the model puffs split with large enough frequency and puffs densely occupy space, they form a slug. This description of the ecological model phenomenology is consistent with previous work [23].

Application to quasi-1D Taylor-Couette flow.—To apply our ecological model to quasi-1D Taylor-Couette flow, we simply note that the forcing on the two systems is different. Pipe flow is pressure driven, and hence kinetic energy is brought in by mean flow from the upstream direction. On the other hand, Taylor-Couette flow is shear driven, which results in uniformly transported kinetic energy from the rotating boundaries to the fluid inside through shear, as shown in of Fig. 1(b). In other words, the mean flow energy in the quasi-1D Taylor-Couette system recovers uniformly with the recovery rate depending on the drive of the rotating boundary, reflected by rotation speed ω. As a result, there is no energy depletion zone in quasi-1D Taylor-Couette flow, and hence the mean flow energy level no longer sets a strong constraint on the growth rate of turbulence.

To model the difference in the driving, we simply replace the local nutrient recovery reaction $\phi \xrightarrow{g} N_i$ with a global one that reflects the global recovery of mean flow energy—when the nutrient growth reaction is triggered, nutrient N no longer just spontaneously grows on a specific site but instead grows uniformly on all sites, unless the site capacity is reached locally. Again, we impose a limited site capacity for nutrients to represent the upper bound for mean flow energy. All the other features of the model for pipe are kept the same.

Space-time plots generated by the PP model below, at, and above the critical point are shown in Fig. 4, replicating the experimental results in quasi-1D Taylor-Couette geometry [6]. Below the critical point, the initial patches of prey B decay, and the system eventually enters an absorbing
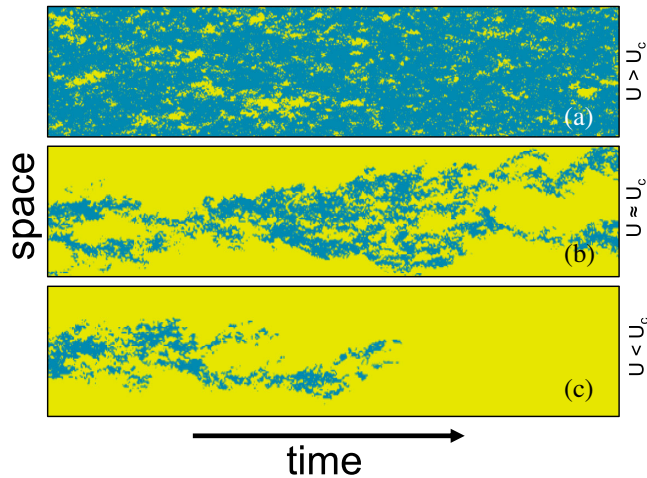
FIG. 4. Space-time plot of laminar-turbulent transition as a function of U (i.e., Reynolds number) generated by the PP model in quasi-1D Taylor-Couette flow. Turbulence (in blue) is represented by the prey density B, generated by Monte Carlo simulation on a 2D lattice of size 20×3000 (a) below the critical point $U = 0.0135$, (b) at the critical point $U = 0.01425$, and (c) above the critical point $U = 0.0165$. Yellow represents the laminar phase locally unoccupied by the prey. Density of prey is binarized according to whether it is larger than $0.065\times$ maximum density of prey.

state with the extinction of B. At the critical point, B is sustained and exhibits scale-invariant fractal structure. Above the critical point, B begins to occupy a portion of the system at long times. The resulting spatiotemporal distribution of turbulence follows the DP pattern clearly seen in quasi-1D Taylor-Couette flow experiments [6].

[1] S. K. Nath and B. Mukhopadhyay, Astrophys. J. **830,** 86 (2016).
[2] P. Manneville, Mech. Eng. Rev. **3,** 15 (2016).
[3] O. Reynolds, Phil. Trans. R. Soc. London 935, 174 (1883).10.1098/rstl.1883.0029
[4] K. Avila, D. Moxey, A. de Lozar, M. Avila, D. Barkley, and B. Hof, Science **333,** 192 (2011).
[5] D. Barkley, B. Song, V. Mukund, G. Lemoult, M. Avila, and B. Hof, Nature (London) **526,** 550 (2015).
[6] G. Lemoult, L. Shi, K. Avila, S. V. Jalikop, M. Avila, and B. Hof, Nat. Phys. **12,** 254 (2016).
[7] Y. Pomeau, Physica (Amsterdam) **23D,** 3 (1986).
[8] D. Barkley, Phys. Rev. E **84,** 016309 (2011).
[9] H.-Y. Shih, T.-L. Hsieh, and N. Goldenfeld, Nat. Phys. **12,** 245 (2016).
[10] P. Manneville, Eur. J. Mech. B/Fluids **49,** 345 (2015).
[11] M. Chantry, L. S. Tuckerman, and D. Barkley, J. Fluid Mech. **824** (2017).
[12] N. Goldenfeld, J. Fluid Mech. **830,** 1 (2017).
[13] B. Eckhardt, Physica (Amsterdam) **504A,** 121 (2018).
[14] N. B. Budanur, E. Marensi, A. P. Willis, and B. Hof, Phys. Rev. Fluids **5,** 023903 (2020).
[15] F. Waleffe, Phys. Fluids **9,** 883 (1997).
[16] J. M. Hamilton, J. Kim, and F. Waleffe, J. Fluid Mech. **287,** 317 (1995).
[17] J. Jiménez and A. Pinelli, J. Fluid Mech. **389,** 335 (1999).
[18] F. Mellibovsky, A. Meseguer, T. M. Schneider, and B. Eckhardt, Phys. Rev. Lett. **103,** 054502 (2009).
[19] Y. Duguet, A. Willis, and R. Kerswell, J. Fluid Mech. **663,** 180 (2010).
[20] N. Goldenfeld and H.-Y. Shih, J. Stat. Phys. **167,** 575 (2017).
[21] D. Barkley, Rev. Cubana Fís. **29,** 1 (2012).
[22] D. Barkley, J. Phys. Condens. Matter **318,** 032001 (2011).
[23] D. Barkley, J. Fluid Mech. **803** (2016).
[24] B. Song, D. Barkley, B. Hof, and M. Avila, J. Fluid Mech. **813,** 1045 (2017).
[25] A. J. McKane and T. J. Newman, Phys. Rev. Lett. **94,** 218102 (2005).
[26] P. H. Diamond, Y.-M. Liang, B. A. Carreras, and P. W. Terry, Phys. Rev. Lett. **72,** 2565 (1994).
[27] T. Estrada, C. Hidalgo, T. Happel, and P. H. Diamond, Phys. Rev. Lett. **107,** 245004 (2011).
[28] T. Butler and N. Goldenfeld, Phys. Rev. E **84,** 011112 (2011).
[29] M. Mobilia, I. T. Georgiev, and U. C. Täuber, J. Stat. Phys. **128,** 447 (2007).
[30] D. Moxey and D. Barkley, Proc. Natl. Acad. Sci. U.S.A. **107,** 8091 (2010).
[31] See Supplemental Material at http://link.aps.org/supplemental/10.1103/PhysRevLett.129.034501 for the derivation of the mean-field model from the stochastic model using the van Kampen system size expansion, description of the Monte Carlo simulation and explanation of the dependence of nutrient growth rate g on U.
[32] U. C. Täuber, J. Phys. A **45,** 405002 (2012).
[33] N. Goldenfeld, *Lectures on Phase Transitions and the Renormalization Group* (Addison-Wesley, Reading, MA, 1992).
[34] G. Dee and J. S. Langer, Phys. Rev. Lett. **50,** 383 (1983).
[35] X. Wang, H.-Y. Shih, and N. Goldenfeld (to be published).
[36] A. Kolmogorov, I. Petrovskii, and N. Piscunov, Mosk. Gos. Univ. **1,** 1 (1937).
[37] R. A. Fisher, Ann. Eugen. **7,** 355 (1937).
[38] G. C. Paquette, L.-Y. Chen, N. Goldenfeld, and Y. Oono, Phys. Rev. Lett. **72,** 76 (1994).
[39] N. Goldenfeld, N. Guttenberg, and G. Gioia, Phys. Rev. E **81,** 035304(R) (2010).

Supplementary Material for "Stochastic model for quasi-one-dimensional transitional turbulence with stream-wise shear interactions"

Xueying Wang[1], Hong-Yan Shih[2] and Nigel Goldenfeld[1,3]

[1]*Department of Physics, University of Illinois at Urbana-Champaign,*

Loomis Laboratory of Physics, 1110 West Green Street, Urbana, Illinois, 61801-3080

[2]*Institute of Physics, Academia Sinica, Taipei 10617, Taiwan*

[3]*Department of Physics, University of California, San Diego, 9500 Gilman Drive, La Jolla, CA 92093, USA*

This document contains details of calculations for:

- Derivation of the mean field limit of the stochastic model, from which the inset of Fig. 3 in the main text is calculated.

- Description of the Monte Carlo simulation for Figures (2) and (3) of the main paper

- Explanation of the dependence of nutrient growth rate g on U.

I. DERIVATION OF STOCHASTIC HYDRODYNAMICS

In this section, we derive the stochastic partial differential equations (PDEs) in the main text, starting from the stochastic individual-level reactions that take place in the system, which are,

$$
\begin{aligned}
& A_i \xrightarrow{d_A} \phi, \;\; B_i \xrightarrow{d_B} \phi, \;\; A_i + B_j \xrightarrow[<ij>]{p/V} A_i + A_j, \\
& B_i + N_j \xrightarrow[<ij>]{b/V} B_i + B_j, \;\; B_i \xrightarrow{m} A_i, \\
& A_i \xrightarrow[<ij>]{D_A} A_j, \;\; B_i \xrightarrow[<ij>]{D_B} B_j, \;\; \phi \xrightarrow{g} N_i \\
& 2A_i \xrightarrow{c_A/V} A_i, \;\; 2B_i \xrightarrow{c_B/V} B_i \\
& N_i \xrightarrow[prob.=1]{speed=U} N_{i+1}.
\end{aligned}
\tag{S.1}
$$
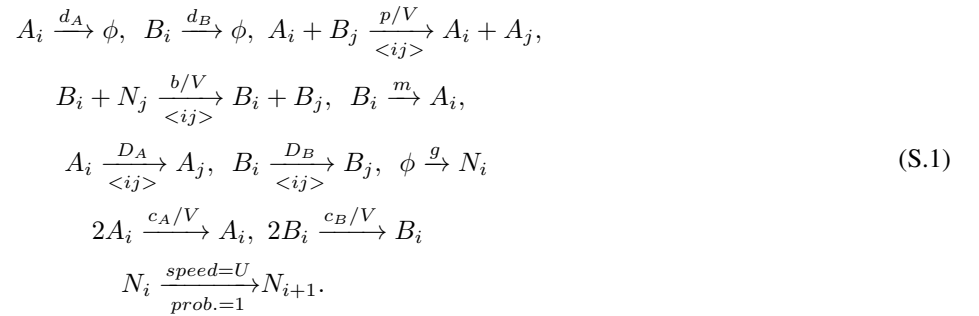
In the continuum limit, the change of number of A, B and N particles with space can be written as functions of space x as $N_A(x)$, $N_B(x)$ and $N_N(x)$. We coarse-grain the particle number and introduce a coarse-grained particle density centered at x over a length scale K with a uniform kernel.

$$
\begin{aligned}
A(x) &= \frac{1}{K} \int_{-K/2}^{K/2} N_A(x+y)dy, \\
B(x) &= \frac{1}{K} \int_{-K/2}^{K/2} N_B(x+y)dy, \\
N(x) &= \frac{1}{K} \int_{-K/2}^{K/2} N_N(x+y)dy,
\end{aligned}
\tag{S.2}
$$

We define the lattice density operator E_x and E_x^{-1} acting on a functional $f[M(y)]$ as,

$$E_x f[M(y)] = f(M(y) + \Delta\delta(y-x)),$$
$$E_x^{-1} f[M(y)] = f(M(y) - \Delta\delta(y-x)). \tag{S.3}$$

where $\Delta = 1/K$, and $M(x)$ denotes the coarse-grained particle number at x. $M(x)$ could be $A(x)$, $B(x)$ or $N(x)$. The master equation can then be written as,

$$
\begin{aligned}
\partial_t P(A,B,N;t) = & \int \left[d_A(E_x^A - 1)A(x,t) + d_B\left(E_x^B - 1\right)B(x,t)\right]P(A,B,N;t)dx \\
& + \iint p/V\left(E_y^B\left(E_x^A\right)^{-1} - 1\right)A(x,t)B(y,t)\delta(x-y-\epsilon)P(A,B,N;t)dxdy \\
& + \iint p/V\left(E_y^B\left(E_x^A\right)^{-1} - 1\right)A(x,t)B(y,t)\delta(x-y+\epsilon)P(A,B,N;t)dxdy \\
& + \iint b/V\left(E_y^N\left(E_x^B\right)^{-1} - 1\right)N(x,t)B(y,t)\delta(x-y-\epsilon)P(A,B,N;t)dxdy \\
& + \iint b/V\left(E_y^N\left(E_x^B\right)^{-1} - 1\right)N(x,t)B(y,t)\delta(x-y+\epsilon)P(A,B,N;t)dxdy \\
& + \int m\left(E_x^B\left(E_x^A\right)^{-1} - 1\right)B(x,t)P(A,B,N;t)dx \\
& + \iint D_A\left(E_y^A\left(E_x^A\right)^{-1} - 1\right)A(y,t)\delta(x-y+\epsilon)P(A,B,N;t)dxdy \\
& + \iint D_A\left(E_y^A\left(E_x^A\right)^{-1} - 1\right)A(y,t)\delta(x-y-\epsilon)P(A,B,N;t)dxdy \\
& + \iint D_B\left(E_y^B\left(E_x^B\right)^{-1} - 1\right)B(y,t)\delta(x-y+\epsilon)P(A,B,N;t)dxdy \\
& + \iint D_B\left(E_y^B\left(E_x^B\right)^{-1} - 1\right)B(y,t)\delta(x-y-\epsilon)P(A,B,N;t)dxdy \\
& + \int [g\left(\left(E_x^N\right)^{-1} - 1\right)(V-N) + c_A/V\left(E_x^A - 1\right)A^2(x,t)]P(A,B,N;t)dx \\
& + \int c_B/V\left(E_x^B - 1\right)B^2(x,t)P(A,B,N;t)dx,
\end{aligned}
\tag{S.4}
$$

where V is site capacity of nutrient and also defined as system size and ϵ is lattice spacing. Note that the predatory, birth and diffusion reaction are nearest-neighbour reactions, and the reaction is symmetric in space (i.e. the probability of the reaction occurring on left nearest neighbour site and on the right nearest neighbour site is the same). That is why for the terms in equation (S.4) that corresponds to each of these reactions, there is a term with $\delta(x-y+\epsilon)$ (left nearest neighbour), and another term with $\delta(x-y-\epsilon)$ (right nearest neighbour). The width of the pipe is much smaller than its length, so we treat the pipe as a quasi-one-dimensional system here, with the position parameter x and y being scalars corresponding to length of the pipe.

Applying van Kampen's expansion and neglecting higher order terms (h.o.t.) beyond second order, we get,

$$
\begin{aligned}
E_x^{A/B/N} M(y,t) &= 1 + \frac{1}{\sqrt{V}}\frac{\partial}{\partial \xi_{A/B/N}(x,t)} + \frac{1}{2V}\frac{\partial^2}{\partial \xi_{A/B/N}(x,t)^2} + h.o.t. \\
(E_x^{A/B/N})^{-1} M(y,t) &= 1 - \frac{1}{\sqrt{V}}\frac{\partial}{\partial \xi_{A/B/N}(x,t)} + \frac{1}{2V}\frac{\partial^2}{\partial \xi_{A/B/N}(x,t)^2} + h.o.t. \\
M(x,t) &= V\rho_{A/B/N}(x,t) + \sqrt{V}\xi_{A/B/N}(x,t) + h.o.t. \\
P(A,B,C;t) &\to \Pi(\xi_A,\xi_B,\xi_N;t)
\end{aligned}
\tag{S.5}
$$

Equation (S.4) becomes,

$$
\begin{aligned}
LHS =& \frac{\partial \Pi}{\partial t} - \sqrt{V} \frac{\partial \Pi}{\partial \xi_A} \frac{\partial \rho_A}{\partial t} - \sqrt{V} \frac{\partial \Pi}{\partial \xi_B} \frac{\partial \rho_B}{\partial t} - \sqrt{V} \frac{\partial \Pi}{\partial \xi_N} \frac{\partial \rho_N}{\partial t} \\
RHS =& \frac{1}{\sqrt{V}} \int \frac{\partial}{\partial \xi_A(x,t)} d_A(V\rho_A(x,t) + \sqrt{V}\xi_A(x,t))\Pi dx + \frac{1}{2V} \int \frac{\partial^2}{\partial \xi_A(x,t)^2} d_A(V\rho_A(x,t) + \sqrt{V}\xi_A(x,t))\Pi dx \\
&+ \frac{1}{\sqrt{V}} \int \frac{\partial}{\partial \xi_B(x,t)} d_B(V\rho_B(x,t) + \sqrt{V}\xi_B(x,t))\Pi dx + \frac{1}{2V} \int \frac{\partial^2}{\partial \xi_B(x,t)^2} d_B(V\rho_B(x,t) + \sqrt{V}\xi_B(x,t))\Pi dx \\
&+ \frac{1}{\sqrt{V}} \int [\frac{\partial}{\partial \xi_B(x,t)} p/V (V\rho_A(x-\epsilon,t) + \sqrt{V}\xi_A(x-\epsilon,t))(V\rho_B(x,t) + \sqrt{V}\xi_B(x,t))]\Pi dx \\
&- \frac{1}{\sqrt{V}} \int [\frac{\partial}{\partial \xi_A(x,t)} p/V (V\rho_A(x-\epsilon,t) + \sqrt{V}\xi_A(x-\epsilon,t))(V\rho_B(x,t) + \sqrt{V}\xi_B(x,t))]\Pi dx \\
&+ \frac{1}{2V} \int [\frac{\partial^2}{\partial \xi_A(x,t)^2} p/V (V\rho_A(x-\epsilon,t) + \sqrt{V}\xi_A(x-\epsilon,t))(V\rho_B(x,t) + \sqrt{V}\xi_B(x,t))]\Pi dx \\
&+ \frac{1}{2V} \int [\frac{\partial^2}{\partial \xi_B(x,t)^2} p/V (V\rho_A(x-\epsilon,t) + \sqrt{V}\xi_A(x-\epsilon,t))(V\rho_B(x,t) + \sqrt{V}\xi_B(x,t))]\Pi dx \\
&- \frac{1}{V} \int [\frac{\partial^2}{\partial \xi_A(x,t)\partial \xi_B(x,t)} p/V (V\rho_A(x-\epsilon,t) + \sqrt{V}\xi_A(x-\epsilon,t))(V\rho_B(x,t) + \sqrt{V}\xi_B(x,t))]\Pi dx \\
&+ \frac{1}{\sqrt{V}} \int [\frac{\partial}{\partial \xi_B(x,t)} p/V (V\rho_A(x+\epsilon,t) + \sqrt{V}\xi_A(x+\epsilon,t))(V\rho_B(x,t) + \sqrt{V}\xi_B(x,t))]\Pi dx \\
&- \frac{1}{\sqrt{V}} \int [\frac{\partial}{\partial \xi_A(x,t)} p/V (V\rho_A(x+\epsilon,t) + \sqrt{V}\xi_A(x+\epsilon,t))(V\rho_B(x,t) + \sqrt{V}\xi_B(x,t))]\Pi dx \\
&+ \frac{1}{2V} \int [\frac{\partial^2}{\partial \xi_A(x,t)^2} p/V (V\rho_A(x+\epsilon,t) + \sqrt{V}\xi_A(x+\epsilon,t))(V\rho_B(x,t) + \sqrt{V}\xi_B(x,t))]\Pi dx \\
&+ \frac{1}{2V} \int [\frac{\partial^2}{\partial \xi_B(x,t)^2} p/V (V\rho_A(x+\epsilon,t) + \sqrt{V}\xi_A(x+\epsilon,t))(V\rho_B(x,t) + \sqrt{V}\xi_B(x,t))]\Pi dx \\
&- \frac{1}{V} \int [\frac{\partial^2}{\partial \xi_A(x,t)\partial \xi_B(x,t)} p/V (V\rho_A(x+\epsilon,t) + \sqrt{V}\xi_A(x+\epsilon,t))(V\rho_B(x,t) + \sqrt{V}\xi_B(x,t))]\Pi dx \\
&+ \frac{1}{\sqrt{V}} \int [\frac{\partial}{\partial \xi_N(x,t)} b/V (V\rho_B(x-\epsilon,t) + \sqrt{V}\xi_B(x-\epsilon,t))(V\rho_N(x,t) + \sqrt{V}\xi_N(x,t))]\Pi dx \\
&- \frac{1}{\sqrt{V}} \int [\frac{\partial}{\partial \xi_B(x,t)} b/V (V\rho_B(x-\epsilon,t) + \sqrt{V}\xi_B(x-\epsilon,t))(V\rho_N(x,t) + \sqrt{V}\xi_N(x,t))]\Pi dx \\
&+ \frac{1}{2V} \int [\frac{\partial^2}{\partial \xi_N(x,t)^2} b/V (V\rho_B(x-\epsilon,t) + \sqrt{V}\xi_B(x-\epsilon,t))(V\rho_N(x,t) + \sqrt{V}\xi_N(x,t))]\Pi dx \\
&+ \frac{1}{2V} \int [\frac{\partial^2}{\partial \xi_B(x,t)^2} b/V (V\rho_B(x-\epsilon,t) + \sqrt{V}\xi_B(x-\epsilon,t))(V\rho_N(x,t) + \sqrt{V}\xi_N(x,t))]\Pi dx \\
&- \frac{1}{V} \int [\frac{\partial^2}{\partial \xi_N(x,t)\partial \xi_B(x,t)} b/V (V\rho_B(x-\epsilon,t) + \sqrt{V}\xi_B(x-\epsilon,t))(V\rho_N(x,t) + \sqrt{V}\xi_N(x,t))]\Pi dx \\
&+ \frac{1}{\sqrt{V}} \int [\frac{\partial}{\partial \xi_N(x,t)} b/V (V\rho_B(x+\epsilon,t) + \sqrt{V}\xi_B(x+\epsilon,t))(V\rho_N(x,t) + \sqrt{V}\xi_N(x,t))]\Pi dx \\
&- \frac{1}{\sqrt{V}} [\frac{\partial}{\partial \xi_B(x,t)} b/V (V\rho_B(x+\epsilon,t) + \sqrt{V}\xi_B(x+\epsilon,t))(V\rho_N(x,t) + \sqrt{V}\xi_N(x,t))]\Pi dx \\
&+ \frac{1}{2V} \int [\frac{\partial^2}{\partial \xi_N(x,t)^2} b/V (V\rho_B(x+\epsilon,t) + \sqrt{V}\xi_B(x+\epsilon,t))(V\rho_N(x,t) + \sqrt{V}\xi_N(x,t))]\Pi dx \\
&+ \frac{1}{2V} \int [\frac{\partial^2}{\partial \xi_B(x,t)^2} b/V (V\rho_B(x+\epsilon,t) + \sqrt{V}\xi_B(x+\epsilon,t))(V\rho_N(x,t) + \sqrt{V}\xi_N(x,t))]\Pi dx \\
&- \frac{1}{V} \int [\frac{\partial^2}{\partial \xi_N(x,t)\partial \xi_B(x,t)} b/V (V\rho_B(x+\epsilon,t) + \sqrt{V}\xi_B(x+\epsilon,t))(V\rho_N(x,t) + \sqrt{V}\xi_N(x,t))]\Pi dx
\end{aligned}
$$

(S.6)

$$+ \frac{1}{\sqrt{V}} \int [\frac{\partial}{\partial \xi_B(x,t)} m(V\rho_B(x,t) + \sqrt{V}\xi_B(x,t))]\Pi dx$$

$$- \frac{1}{\sqrt{V}} \int [\frac{\partial}{\partial \xi_A(x,t)} m(V\rho_B(x,t) + \sqrt{V}\xi_B(x,t))]\Pi dx$$

$$+ \frac{1}{2V} \int [\frac{\partial^2}{\partial \xi_B(x,t)^2} m(V\rho_B(x,t) + \sqrt{V}\xi_B(x,t))]\Pi dx + \frac{1}{2V} \int [\frac{\partial^2}{\partial \xi_A(x,t)^2} m(V\rho_B(x,t) + \sqrt{V}\xi_B(x,t))]\Pi dx$$

$$- \frac{1}{V} \int [\frac{\partial^2}{\partial \xi_A(x,t)\partial \xi_B(x,t)} m(V\rho_B(x,t) + \sqrt{V}\xi_B(x,t))]\Pi dx$$

$$+ \frac{1}{\sqrt{V}} \int \frac{\partial}{\partial \xi_A(x,t)} D_A[(V\rho_A(x,t) + \sqrt{V}\xi_A(x,t)) - (V\rho_A(x+\epsilon,t) + \sqrt{V}\xi_A(x+\epsilon,t))]\Pi dx$$

$$+ \frac{1}{2V} \int \frac{\partial^2}{\partial \xi_A(x,t)^2} D_A[(V\rho_A(x,t) + \sqrt{V}\xi_A(x,t)) + (V\rho_A(x+\epsilon,t) + \sqrt{V}\xi_A(x+\epsilon,t))]\Pi dx$$

$$- \frac{1}{V} \iint \frac{\partial^2}{\partial \xi_A(x,t)\partial \xi_A(y,t)} D_A(V\rho_A(y,t) + \sqrt{V}\xi_A(y,t))\delta(x-y+\epsilon)\Pi dxdy$$

$$+ \frac{1}{\sqrt{V}} \int \frac{\partial}{\partial \xi_A(x,t)} D_A[(V\rho_A(x,t)\sqrt{V}\xi_A(x,t)) - (V\rho_A(x-\epsilon,t) + \sqrt{V}\xi_A(x-\epsilon,t))]\Pi dx$$

$$+ \frac{1}{2V} \int \frac{\partial^2}{\partial \xi_A(x,t)^2} D_A[(V\rho_A(x,t) + \sqrt{V}\xi_A(x,t)) + (V\rho_A(x-\epsilon,t) + \sqrt{V}\xi_A(x-\epsilon,t))]\Pi dx$$

$$- \frac{1}{V} \iint \frac{\partial^2}{\partial \xi_A(x,t)\partial \xi_A(y,t)} D_A(V\rho_A(y,t) + \sqrt{V}\xi_A(y,t))\delta(x-y-\epsilon)\Pi dxdy$$

$$+ \frac{1}{\sqrt{V}} \int \frac{\partial}{\partial \xi_A(x,t)} D_B[(V\rho_B(x,t) + \sqrt{V}\xi_B(x,t)) - (V\rho_B(x+\epsilon,t) + \sqrt{V}\xi_B(x+\epsilon,t))]\Pi dx$$

$$+ \frac{1}{2V} \int \frac{\partial^2}{\partial \xi_B(x,t)^2} D_B[(V\rho_B(x,t) + \sqrt{V}\xi_B(x,t)) + (V\rho_B(x+\epsilon,t) + \sqrt{V}\xi_B(x+\epsilon,t))]\Pi dx$$

$$- \frac{1}{V} \iint \frac{\partial^2}{\partial \xi_B(x,t)\partial \xi_B(y,t)} D_B(V\rho_B(y,t) + \sqrt{V}\xi_B(y,t))\delta(x-y+\epsilon)\Pi dxdy$$

$$+ \frac{1}{\sqrt{V}} \int \frac{\partial}{\partial \xi_B(x,t)} D_B[(V\rho_B(x,t) + \sqrt{V}\xi_B(x,t)) - (V\rho_B(x-\epsilon,t) + \sqrt{V}\xi_B(x-\epsilon,t))]\Pi dx$$

$$+ \frac{1}{2V} \int \frac{\partial^2}{\partial \xi_B(x,t)^2} D_B[(V\rho_B(x,t) + \sqrt{V}\xi_B(x,t)) + (V\rho_B(x-\epsilon,t) + \sqrt{V}\xi_B(x-\epsilon,t))]\Pi dx$$

$$- \frac{1}{V} \iint \frac{\partial^2}{\partial \xi_B(x,t)\partial \xi_B(y,t)} D_B(V\rho_B(y,t) + \sqrt{V}\xi_B(y,t))\delta(x-y-\epsilon)\Pi dxdy$$

$$- \frac{1}{\sqrt{V}} \int \frac{\partial}{\partial \xi_N(x,t)} g(V - (V\rho_N(x,t) + \sqrt{V}\xi_N(x,t)))\Pi dx$$

$$+ \frac{1}{2V} \int \frac{\partial^2}{\partial \xi_N(x,t)^2} g(V - (V\rho_N(x,t) + \sqrt{V}\xi_N(x,t)))\Pi dx$$

$$+ \frac{1}{\sqrt{V}} \int \frac{\partial}{\partial \xi_A(x,t)} c_A/V(V\rho_A(x,t) + \sqrt{V}\xi_A(x,t))^2\Pi dx + \frac{1}{2V} \int \frac{\partial^2}{\partial \xi_A(x,t)^2} c_A/V(V\rho_A(x,t) + \sqrt{V}\xi_A(x,t))^2\Pi dx$$

$$+ \frac{1}{\sqrt{V}} \int \frac{\partial}{\partial \xi_B(x,t)} c_B/V(V\rho_B(x,t) + \sqrt{V}\xi_B(x,t))^2\Pi dx + \frac{1}{2V} \int \frac{\partial^2}{\partial \xi_B(x,t)^2} c_B/V(V\rho_B(x,t) + \sqrt{V}\xi_B(x,t))^2\Pi dx$$

$$\text{(S.7)}$$

Expanding out all the terms and keeping terms up to second order, we obtain:

$$RHS = \sqrt{V}[\int d_A\rho_A(x,t) \frac{\partial}{\partial \xi_A(x,t)} \Pi dx] + \sqrt{V}[\int d_B\rho_B(x,t) \frac{\partial}{\partial \xi_B(x,t)} \Pi dx]$$

$$+ [\int \frac{\partial}{\partial \xi_A(x,t)} d_A\xi_A(x,t)\Pi dx + \frac{d_A}{2}\rho_A \int \frac{\partial^2}{\partial \xi_A(x,t)^2}\Pi dx] + [\int \frac{\partial}{\partial \xi_B(x,t)} d_B\xi_B(x,t)\Pi dx + \frac{d_B}{2}\rho_B \int \frac{\partial^2}{\partial \xi_B(x,t)^2}\Pi dx]$$

$$\text{(S.8)}$$

$$+ \sqrt{V} \int p \rho_A(x-\epsilon,t) \rho_B(x,t) \frac{\partial}{\partial \xi_B(x,t)} \Pi dx - \sqrt{V} \int p \rho_A(x-\epsilon,t) \rho_B(x,t) \frac{\partial}{\partial \xi_A(x,t)} \Pi dx$$

$$+ \sqrt{V} \int p \rho_A(x+\epsilon,t) \rho_B(x,t) \frac{\partial}{\partial \xi_B(x,t)} \Pi dx - \sqrt{V} \int p \rho_A(x+\epsilon,t) \rho_B(x,t) \frac{\partial}{\partial \xi_A(x,t)} \Pi dx$$

$$+ \int p \rho_A(x-\epsilon,t) \frac{\partial}{\partial \xi_B(x,t)} \xi_B(x,t) \Pi dt + \int p \rho_B(x,t) \xi_A(x-\epsilon,t) \frac{\partial}{\partial \xi_B(x,t)} \Pi dt$$

$$- \int p \rho_A(x-\epsilon,t) \frac{\partial}{\partial \xi_A(x,t)} \xi_B(x,t) \Pi dt - \int p \rho_B(x,t) \frac{\partial}{\partial \xi_A(x,t)} \xi_A(x-\epsilon,t) \Pi dt$$

$$+ \frac{1}{2} \int p \rho_A(x-\epsilon,t) \rho_B(x,t) \frac{\partial^2}{\partial \xi_A(x,t)^2} \Pi dx + \frac{1}{2} \int p \rho_A(x-\epsilon,t) \rho_B(x,t) \frac{\partial^2}{\partial \xi_B(x,t)^2} \Pi dx$$

$$- \int p \rho_A(x-\epsilon,t) \rho_B(x,t) \frac{\partial^2}{\partial \xi_A(x,t) \partial \xi_B(x,t)} \Pi dx$$

$$+ \int p \rho_A(x+\epsilon,t) \frac{\partial}{\partial \xi_B(x,t)} \xi_B(x,t) \Pi dt + \int p \rho_B(x,t) \xi_A(x+\epsilon,t) \frac{\partial}{\partial \xi_B(x,t)} \Pi dt$$

$$- \int p \rho_A(x+\epsilon,t) \frac{\partial}{\partial \xi_A(x,t)} \xi_B(x,t) \Pi dt - \int p \rho_B(x,t) \frac{\partial}{\partial \xi_A(x,t)} \xi_A(x+\epsilon,t) \Pi dt$$

$$+ \frac{1}{2} \int p \rho_A(x+\epsilon,t) \rho_B(x,t) \frac{\partial^2}{\partial \xi_A(x,t)^2} \Pi dx + \frac{1}{2} \int p \rho_A(x+\epsilon,t) \rho_B(x,t) \frac{\partial^2}{\partial \xi_B(x,t)^2} \Pi dx$$

$$- \int p \rho_A(x+\epsilon,t) \rho_B(x,t) \frac{\partial^2}{\partial \xi_A(x,t) \partial \xi_B(x,t)} \Pi dx$$

$$+ \sqrt{V} \int b \rho_B(x-\epsilon,t) \rho_N(x,t) \frac{\partial}{\partial \xi_N(x,t)} \Pi dx - \sqrt{V} \int b \rho_B(x-\epsilon,t) \rho_N(x,t) \frac{\partial}{\partial \xi_B(x,t)} \Pi dx$$

$$+ \sqrt{V} \int b \rho_B(x+\epsilon,t) \rho_N(x,t) \frac{\partial}{\partial \xi_N(x,t)} \Pi dx - \sqrt{V} \int b \rho_B(x+\epsilon,t) \rho_N(x,t) \frac{\partial}{\partial \xi_B(x,t)} \Pi dx$$

$$+ \int b \rho_B(x-\epsilon,t) \frac{\partial}{\partial \xi_N(x,t)} \xi_N(x,t) \Pi dt + \int b \rho_N(x,t) \xi_B(x-\epsilon,t) \frac{\partial}{\partial \xi_N(x,t)} \Pi dt$$

$$- \int b \rho_B(x-\epsilon,t) \frac{\partial}{\partial \xi_B(x,t)} \xi_N(x,t) \Pi dt - \int b \rho_N(x,t) \frac{\partial}{\partial \xi_B(x,t)} \xi_B(x-\epsilon,t) \Pi dt$$

$$+ \int \frac{1}{2} b \rho_B(x-\epsilon,t) \rho_N(x,t) \frac{\partial^2}{\partial \xi_B(x,t)^2} \Pi dx + \int \frac{1}{2} b \rho_B(x-\epsilon,t) \rho_N(x,t) \frac{\partial^2}{\partial \xi_N(x,t)^2} \Pi dx$$

$$- \int b \rho_B(x-\epsilon,t) \rho_N(x,t) \frac{\partial^2}{\partial \xi_B(x,t) \partial \xi_N(x,t)} \Pi dx$$

$$+ \int b \rho_B(x+\epsilon,t) \frac{\partial}{\partial \xi_N(x,t)} \xi_N(x,t) \Pi dt + \int b \rho_N(x,t) \xi_B(x+\epsilon,t) \frac{\partial}{\partial \xi_N(x,t)} \Pi dt$$

$$- \int b \rho_B(x+\epsilon,t) \frac{\partial}{\partial \xi_B(x,t)} \xi_N(x,t) \Pi dt - \int b \rho_N(x,t) \frac{\partial}{\partial \xi_B(x,t)} \xi_B(x+\epsilon,t) \Pi dt$$

$$+ \int \frac{1}{2} b \rho_B(x+\epsilon,t) \rho_N(x,t) \frac{\partial^2}{\partial \xi_B(x,t)^2} \Pi dx + \int \frac{1}{2} b \rho_B(x+\epsilon,t) \rho_N(x,t) \frac{\partial^2}{\partial \xi_N(x,t)^2} \Pi dx$$

$$- \int b \rho_B(x+\epsilon,t) \rho_N(x,t) \frac{\partial^2}{\partial \xi_B(x,t) \partial \xi_N(x,t)} \Pi dx$$

$$+ \sqrt{V} \int m \rho_B(x,t) \frac{\partial}{\partial \xi_B(x,t)} \Pi dx - \sqrt{V} \int m \rho_B(x,t) \frac{\partial}{\partial \xi_A(x,t)} \Pi dx + m \int \frac{\partial}{\partial \xi_B} \xi_B \Pi dx - m \int \xi_B \frac{\partial}{\partial \xi_A} \Pi dx$$

$$+ \frac{1}{2} \int m \rho_B(x,t) \frac{\partial^2}{\partial \xi_B(x,t)^2} \Pi dx + \frac{1}{2} \int m \rho_B(x,t) \frac{\partial^2}{\partial \xi_A(x,t)^2} \Pi dx - \int m \rho_B(x,t) \frac{\partial^2}{\partial \xi_A(x,t) \partial \xi_B(x,t)} \Pi dx$$

$$+ \sqrt{V} \int D_A(\rho_A(x,t) - \rho_A(x+\epsilon,t)) \frac{\partial}{\partial \xi_A(x,t)} \Pi dx + \int \frac{\partial}{\partial \xi_A(x,t)} D_A(\xi_A(x,t) - \xi_A(x+\epsilon,t)) \Pi dx$$

$$+ \frac{1}{2} \int D_A(\rho_A(x,t) + \rho_A(x+\epsilon,t)) \frac{\partial^2}{\partial \xi_A(x,t)^2} \Pi dx - \iint D_A \rho_A(y,t) \delta(x-y+\epsilon) \frac{\partial^2}{\partial \xi_A(x,t) \partial \xi_A(y,t)} \Pi dx dy$$

$$+ \sqrt{V} \int D_A(\rho_A(x,t) - \rho_A(x-\epsilon,t)) \frac{\partial}{\partial \xi_A(x,t)} \Pi dx + \int \frac{\partial}{\partial \xi_A(x,t)} D_A(\xi_A(x,t) - \xi_A(x-\epsilon,t)) \Pi dx$$

$$+ \frac{1}{2} \int D_A(\rho_A(x,t) + \rho_A(x-\epsilon,t)) \frac{\partial}{\partial \xi_A(x,t)^2} \Pi dx - \iint D_A \rho_A(y,t) \delta(x-y-\epsilon) \frac{\partial^2}{\partial \xi_A(x,t) \partial \xi_A(y,t)} \Pi dx dy$$

$$\text{(S.9)}$$

5

$$+ \sqrt{V} \int D_B(\rho_B(x,t) - \rho_B(x+\epsilon,t)) \frac{\partial}{\partial \xi_B(x,t)} \Pi dx + \int \frac{\partial}{\partial \xi_B(x,t)} D_B(\xi_B(x,t) - \xi_B(x+\epsilon,t)) \Pi dx$$

$$+ \frac{1}{2} \int D_B(\rho_B(x,t) - \rho_B(x+\epsilon,t)) \frac{\partial}{\partial \xi_B(x,t)} \Pi dx - \iint D_B \rho_B(y,t) \delta(x-y+\epsilon) \frac{\partial^2}{\partial \xi_B(x,t) \partial \xi_B(y,t)} \Pi dxdy$$

$$+ \sqrt{V} \int D_B(\rho_B(x,t) - \rho_B(x-\epsilon,t)) \frac{\partial}{\partial \xi_B(x,t)} \Pi dx + \int \frac{\partial}{\partial \xi_B(x,t)} D_B(\xi_B(x,t) - \xi_B(x-\epsilon,t)) \Pi dx$$

$$+ \frac{1}{2} \int D_B(\rho_B(x,t) - \rho_B(x-\epsilon,t)) \frac{\partial}{\partial \xi_B(x,t)} \Pi dx - \iint D_B \rho_B(y,t) \delta(x-y-\epsilon) \frac{\partial^2}{\partial \xi_B(x,t) \partial \xi_B(y,t)} \Pi dxdy$$

$$- \sqrt{V} \int g(1 - \rho_N(x,t)) \frac{\partial}{\partial \xi_N(x,t)} \Pi dx + \int g \frac{\partial}{\partial \xi_N(x,t)} \xi_N(x,t) \Pi dx + \frac{1}{2} \int g(1 - \rho_N(x,t)) \frac{\partial^2}{\partial \xi_N(x,t)^2} \Pi dx$$

$$+ \sqrt{V} c_A \rho_A(x,t)^2 \int \frac{\partial}{\partial \xi_A(x,t)} \Pi dx + \sqrt{V} c_B \rho_B(x,t)^2 \int \frac{\partial}{\partial \xi_B(x,t)} \Pi dx$$

$$+ c_A \rho_A(x,t) \int \frac{\partial}{\partial \xi_A(x,t)} \xi_A(x,t) \Pi dx + \frac{1}{2} c_A \rho_A(x,t)^2 \int \frac{\partial^2}{\partial \xi_A(x,t)^2} \Pi dx$$

$$+ c_B \rho_B(x,t) \int \frac{\partial}{\partial \xi_B(x,t)} \xi_B(x,t) \Pi dx + \frac{1}{2} c_B \rho_B(x,t)^2 \int \frac{\partial^2}{\partial \xi_B(x,t)^2} \Pi dx. \tag{S.10}$$

We can then perform a Taylor expansion,

$$\rho(x \pm \epsilon, t) \approx \rho(x,t) \pm \epsilon \partial_x \rho(x,t) + \frac{1}{2} \epsilon^2 \partial_x^2 \rho(x,t). \tag{S.11}$$

and similarly for the $\delta(x-y+\epsilon)$ and $\delta(x-y-\epsilon)$ terms:

$$\iint \frac{\partial^2}{\partial \xi_A(x,t) \partial \xi_A(y,t)} [D_A \rho_A(y,t) \delta(x-y+\epsilon) + D_A \rho_A(y,t) \delta(x-y-\epsilon)] \Pi dxdy$$

$$= \iint \frac{\partial^2}{\partial \xi_A(x,t) \partial \xi_A(y,t)} [D_A \rho_A(x,t) \delta(y-x+\epsilon) + D_A \rho_A(x,t) \delta(y-x-\epsilon)] \Pi dxdy$$

$$= \iint \frac{\partial^2}{\partial \xi_A(x,t) \partial \xi_A(y,t)} \left[D_A \rho_A(x,t)[\delta(y-x) + \epsilon \delta'(y-x) + \frac{\epsilon^2}{2} \delta''(y-x) + \delta(y-x) - \epsilon \delta'(y-x) + \frac{\epsilon^2}{2} \delta''(y-x)] \right] \Pi dxdy$$

$$= \iint \frac{\partial^2}{\partial \xi_A(x,t) \partial \xi_A(y,t)} \left[D_A \delta(y-x)[\rho_A(x,t) - \epsilon \partial_x \rho_A(x,t) + \frac{\epsilon^2}{2} \partial_x^2 \rho_A(x,t) + \rho_A(x,t) + \epsilon \partial_x \rho_A(x,t) + \frac{\epsilon^2}{2} \partial_x^2 \rho_A(x,t)] \right] \Pi dxdy$$

$$= \iint \frac{\partial^2}{\partial \xi_A(x,t) \partial \xi_A(y,t)} D_A[2\rho_A(x,t) + \epsilon^2 \partial_x^2 \rho_A(x,t)] \delta(y-x) \Pi dxdy \tag{S.12}$$

and:

$$\iint \frac{\partial^2}{\partial \rho_B(x,t) \partial \rho_B(y,t)} [D_B \rho_B(y,t) \delta(x-y+\epsilon) + D_B \rho_B(y,t) \delta(x-y-\epsilon)] \Pi dxdy$$

$$= \iint \frac{\partial^2}{\partial \xi_B(x,t) \partial \xi_B(y,t)} D_B[2\rho_B(x,t) + \epsilon^2 \partial_x^2 \rho_B(x,t)] \delta(y-x) \Pi dxdy. \tag{S.13}$$

Collecting the $\sqrt{V}$ terms, we obtain the deterministic PDEs:

$$\frac{\partial \rho_A(x,t)}{\partial t} = -d_A\rho_A(x,t) + 2p\rho_A(x,t)\rho_B(x,t) + p\rho_B(x,t)\epsilon^2\partial_x^2\rho_A(x,t) + m\rho_B(x,t) + D_A\epsilon^2\partial_x^2\rho_A(x,t) - c_A\rho_A(x,t)^2,$$

$$\frac{\partial \rho_B(x,t)}{\partial t} = -d_B\rho_B(x,t) - 2p\rho_A(x,t)\rho_B(x,t) - p\rho_B(x,t)\epsilon^2\partial_x^2\rho_A(x,t) + 2b\rho_B(x,t)\rho_N(x,t) + b\rho_N(x,t)\epsilon^2\partial_x^2\rho_B(x,t)$$

$$- m\rho_B(x,t) + D_B\epsilon^2\partial_x^2\rho_B(x,t) - c_B\rho_B(x,t)^2,$$

$$\frac{\partial \rho_N(x,t)}{\partial t} = -2b\rho_B(x,t)\rho_N(x,t) - b\rho_N(x,t)\epsilon^2\partial_x^2\rho_B(x,t) + g(1 - \rho_N(x,t)).$$

$$\text{(S.14)}$$

From the next order O(1) terms, we obtain:

$$\partial_t\Pi = -\int A_{33}\frac{\partial}{\partial\xi_N(x,t)}\xi_N(x,t)\Pi dx - \int A_{22}\frac{\partial}{\partial\xi_B(x,t)}\xi_B(x,t)\Pi dx - \int A_{11}\frac{\partial}{\partial\xi_A(x,t)}\xi_A(x,t)\Pi dx$$

$$- \int A_{12}\frac{\partial}{\partial\xi_A(x,t)}\xi_B(x,t)\Pi dx - \int A_{21}\frac{\partial}{\partial\xi_B(x,t)}\xi_A(x,t)\Pi dx - \int A_{23}\frac{\partial}{\partial\xi_B(x,t)}\xi_N(x,t)\Pi dx - \int A_{32}\frac{\partial}{\partial\xi_N(x,t)}\xi_B(x,t)\Pi dx$$

$$+ \frac{1}{2}\iint\frac{\partial^2}{\partial\xi_N(x,t)\partial\xi_N(y,t)}B_{33}\Pi dxdy + \frac{1}{2}\iint\frac{\partial^2}{\partial\xi_A(x,t)\partial\xi_A(y,t)}B_{11}\Pi dxdy + \frac{1}{2}\iint\frac{\partial^2}{\partial\xi_B(x,t)\partial\xi_B(y,t)}B_{22}\Pi dxdy$$

$$+ \frac{1}{2}\iint\frac{\partial^2}{\partial\xi_A(x,t)\partial\xi_B(y,t)}B_{12}\Pi dxdy + \frac{1}{2}\iint\frac{\partial^2}{\partial\xi_N(x,t)\partial\xi_B(y,t)}B_{23}\Pi dxdy$$

$$+ \frac{1}{2}\iint\frac{\partial^2}{\partial\xi_A(x,t)\partial\xi_B(y,t)}B_{21}\Pi dxdy + \frac{1}{2}\iint\frac{\partial^2}{\partial\xi_N(x,t)\partial\xi_B(y,t)}B_{32}\Pi dxdy,$$

$$\text{(S.15)}$$

where

$$A_{11} = -d_A + p\rho_B(x,t)(2 + \epsilon^2\partial_x^2) + D_A(\epsilon^2\partial_x^2) - c_A\rho_A(x,t),$$

$$A_{22} = -d_B - p(2\rho_A(x,t) + \epsilon^2\partial_x^2\rho_A(x,t)) + b\rho_N(x,t)(2 + \epsilon^2\partial_x^2) - m + D_B(\epsilon^2\partial_x^2) - c_B\rho_B(x,t) + m,$$

$$A_{33} = -b(2 + \epsilon^2\partial_x^2)\rho_B(x,t) - g$$

$$A_{12} = p(2 + \epsilon^2\partial_x^2)\rho_A(x,t) + m$$

$$A_{21} = -p\rho_B(x,t)(2 + \epsilon^2\partial_x^2)$$

$$A_{23} = b(2 + \epsilon^2\partial_x^2)\rho_B(x,t)$$

$$A_{32} = -b\rho_N(x,t)(2 + \epsilon^2\partial_x^2)$$

$$B_{11} = [d_A\rho_A(x,t) + p\rho_B(x,t)(2 + \epsilon^2\partial_x^2)\rho_A(x,t) + m\rho_B(x,t) - 2D_A(2\rho_A(x,t) + \epsilon^2\partial_x^2\rho_A(x,t)) + 4D_A\rho_A(x,t)$$

$$+ D_A\epsilon^2\partial_x^2\rho_A(x,t) + c_A\rho_A(x,t)^2]\delta(x - y)$$

$$= [d_A\rho_A(x,t) + p\rho_B(x,t)(2 + \epsilon^2\partial_x^2)\rho_A(x,t) + m\rho_B(x,t) + c_A\rho_A(x,t)^2 - D_A\epsilon^2\partial_x^2\rho_A(x,t)]\delta(x - y),$$

$$B_{22} = [d_B\rho_B(x,t) + p\rho_B(x,t)(2 + \epsilon^2\partial_x^2)\rho_A(x,t) + b\rho_N(x,t)(2 + \epsilon^2\partial_x^2)\rho_B(x,t) + m\rho_B(x,t)$$

$$- 2D_B(2\rho_B(x,t) + \epsilon^2\partial_x^2\rho_B(x,t)) + c_B\rho_B(x,t)^2 + 4D_B\rho_A(x,t) + D_B\epsilon^2\partial_x^2\rho_B(x,t)]\delta(x - y)$$

$$= [d_B\rho_B(x,t) + p\rho_B(x,t)(2 + \epsilon^2\partial_x^2)\rho_A(x,t) + b\rho_N(x,t)(2 + \epsilon^2\partial_x^2)\rho_B(x,t) + m\rho_B(x,t) + c_B\rho_B(x,t)^2$$

$$- D_B\epsilon^2\partial_x^2\rho_B(x,t)]\delta(x - y),$$

$$B_{33} = [b\rho_N(x,t)(2 + \epsilon^2\partial_x^2)\rho_B(x,t) + g(1 - \rho_N(x,t))]\delta(x - y),$$

$$B_{12} = B_{21} = [-p\rho_B(x,t)(2 + \epsilon^2\partial_x^2)\rho_A(x,t) - m\rho_B(x,t)]\delta(x - y),$$

$$B_{23} = B_{32} = [-b\rho_N(x,t)(2 + \epsilon^2\partial_x^2)\rho_B(x,t)]\delta(x - y).$$

$$\text{(S.16)}$$

7

The corresponding Langevin equation in the Itô sense can be written as,

$$\partial_t \rho_A = A_{11}\rho_A + A_{12}\rho_B + \eta_A(x,t),$$
$$\partial_t \rho_B = A_{21}\rho_A + A_{22}\rho_B + A_{23}\rho_N + \eta_B(x,t),$$
$$\partial_t \rho_N = A_{32}\rho_B + A_{33}\rho_N + \eta_N(x,t),$$
$$<\eta_A(x,t)\eta_A(x',t')> = B_{11}\delta(t-t'),$$
$$<\eta_B(x,t)\eta_B(x',t')> = B_{22}\delta(t-t'),$$
$$<\eta_N(x,t)\eta_N(x',t')> = B_{33}\delta(t-t'),$$
$$<\eta_A(x,t)\eta_B(x',t')> = <\eta_B(x,t)\eta_A(x',t')> = B_{12}\delta(t-t'),$$
$$<\eta_B(x,t)\eta_N(x',t')> = <\eta_N(x,t)\eta_B(x',t')> = B_{23}\delta(t-t').$$

(S.17)

and

$$A_{11} = -d_A + p\rho_B(2+\partial_x^2) + D_A(\partial_x^2) - c_A\rho_A,$$
$$A_{22} = -d_B - p(2\rho_A + \partial_x^2\rho_A) + b\rho_N(2+\partial_x^2) - m + D_B(\partial_x^2) - c_B\rho_B + m,$$
$$A_{33} = -b(2+\partial_x^2)\rho_B - g$$
$$A_{12} = p(2+\partial_x^2)\rho_A + m$$
$$A_{21} = -p\rho_B(2+\partial_x^2)$$
$$A_{23} = b(2+\partial_x^2)\rho_B$$
$$A_{32} = -b\rho_N(2+\partial_x^2)$$
$$B_{11} = [d_A\rho_A + p\rho_B(2+\partial_x^2)\rho_A + m\rho_B + c_A\rho_A^2 - D_A\partial_x^2\rho_A]\delta(x-y)$$
$$B_{22} = [d_B\rho_B + p\rho_B(2+\partial_x^2)\rho_A + b\rho_N(2+\partial_x^2)\rho_B + m\rho_B + c_B\rho_B^2 - D_B\partial_x^2\rho_B]\delta(x-y)$$
$$B_{33} = [b\rho_N(2+\partial_x^2)\rho_B + g(1-\rho_N)]\delta(x-y),$$
$$B_{12} = [-p\rho_B(2+\partial_x^2)\rho_A - m\rho_B]\delta(x-y),$$
$$B_{23} = [-b\rho_N(2+\partial_x^2)\rho_B]\delta(x-y).$$

(S.18)

Setting the lattice spacing $\epsilon = 1$ and adding in the deterministic advection term, we obtain:

$$\frac{\partial \rho_A}{\partial t} = -d_A\rho_A + 2p\rho_A\rho_B + p\rho_B\partial_x^2\rho_A + m\rho_B + D_A\partial_x^2\rho_A - c_A\rho_A^2,$$
$$\frac{\partial \rho_B}{\partial t} = -d_B\rho_B - 2p\rho_A\rho_B - p\rho_B\partial_x^2\rho_A + 2b\rho_B\rho_N + b\rho_N\partial_x^2\rho_B - m\rho_B + D_B\partial_x^2\rho_B - c_B\rho_B^2,$$
$$\frac{\partial \rho_N}{\partial t} = -U\partial_x^2\rho_N - 2b\rho_B\rho_N - b\rho_N\partial_x^2\rho_B + g(1-\rho_N).$$

(S.19)

The calculation outlined here is systematic but only within the applicability of the van Kampen expansion. This expansion is appropriate when the number of degrees of freedom in all field variables is much larger than unity, so it is sometimes called a system size expansion. In other words, it is a mean field theory. This limit is self-consistent when the ecosystem representing the laminar-turbulent interactions is well-supplied with energy from the mean flow, but will fail to be self-consistent at fronts where the energy is vanishingly small and the number of quanta of the nutrient is of order unity. There is no fully systematic solution to this problem known to us, and we mention the following heuristic considerations to motivate the way that we have

approached making a physically realistic approximation.

Due to the constraint set by the nutrient capacity, densities of predator and prey can be low in some regions of space, and the van Kampen expansion will not reflect the correct growth behavior. Specifically, in the ρ_N equation of equation (S.19), we note that the term $g(1 - \rho_N)$ does not reflect the correct growth behavior under site capacity constraint – without nonlinear terms, the curvature of the growth rate does not vary close to the site capacity, so ρ_N does not saturate close to the upper bound as one would expect based on logistic growth, for example. One way to address this is to ask what would have been obtained in a model that does not impose strict number constraints on site occupancy (so-called "urn" models). The alternative is to impose carrying capacity by adding an additional competition term in the individual-level reactions for the prey; this has the effect of limiting the growth to an emergent value of the carrying capacity which depends on the competition coupling constant [1]. These terms would naturally generate a term such as $-c_N \rho_N^2$ term, and result in:

$$
\begin{aligned}
\frac{\partial \rho_A}{\partial t} &= -d_A \rho_A + 2p\rho_A \rho_B + p\rho_B \partial_x^2 \rho_A + m\rho_B + D_A \partial_x^2 \rho_A - c_A \rho_A^2, \\
\frac{\partial \rho_B}{\partial t} &= -d_B \rho_B - 2p\rho_A \rho_B - p\rho_B \partial_x^2 \rho_A + 2b\rho_B \rho_N + b\rho_N \partial_x^2 \rho_B - m\rho_B + D_B \partial_x^2 \rho_B - c_B \rho_B^2, \\
\frac{\partial \rho_N}{\partial t} &= -U\partial_x \rho_N - 2b\rho_B \rho_N - b\rho_N \partial_x^2 \rho_B + g(1 - \rho_N) - c_N \rho_N^2,
\end{aligned}
\tag{S.20}
$$

which is the final result of the deterministic mean field PDEs for the three trophic level model. Eqn. (S.20) is solved numerically to calculate the mean field front speed in the inset of Fig. 3 of the mean text.

II. ALGORITHM FOR THE MONTE CARLO SIMULATION

The Monte Carlo simulation is performed on a 2D lattice of size 20×3000. We initially perturb the system by randomly generating prey B (with probability $2/5$) and predator A (with probability $2/5$) in a small area of size 20×30 in the middle of the lattice. Simulation results are not sensitive to the initial composition of predator and prey. The number of nutrients upstream of the predator and prey is set to the nutrient site capacity, while the nutrient number is set to zero downstream to avoid the transient growth in prey and predator population at the beginning of the simulation and help the system get to the steady-state faster.

The predator and prey experience rigid wall boundary conditions at the boundary.

During the simulation, the predator and prey may not cross the boundary of the system. For nutrients, however, in addition to having a periodic boundary condition, the number of nutrients is refilled to the site capacity on the left boundary.

The simulation procedure for one time step is as follows,

- A random site is selected. In one time step, 20×3000 lattice sites are selected in total to make sure that every site on the lattice is visited once on average.

- A random number R is generated between 0 and 1. The value of the number R determines which reaction will take place on the selected lattice site. Generate another random number R_1 between 0 and 1. The value of the number R_1 determines whether the selected reaction occurs on the selected site. If $R \leq 1/10$, predator diffusion reaction is selected. And then, if $R_1 \leq 1 - \exp(-D_A \times number\ of\ predator\ on\ the\ lattice)$ (the form of the probability will be derived below), the predator diffusion reaction occurs. One of the predators on the lattice site will hop to one of the four nearest-neighbor sites.

- If $1/10 < R \leq 2/10$, prey diffusion reaction is selected. And then, if $R_1 < 1 - \exp(-D_B \times number\ of\ prey\ on\ the\ lattice)$, the prey diffusion reaction occurs. One of the prey on the lattice site will hop to one of the four nearest-neighbor sites.

- If $2/10 < R \leq 3/10$, prey birth reaction is selected. Then, if $R_1 < 1 - \exp(-b/V \times number\ of\ prey\ on\ the\ lattice \times number\ of\ nutrient\ on\ the\ lattice)$ (V is system size, a parameter that controls the strength of noise), the prey birth reaction occurs. One of the prey on the lattice site generates another prey on one of the four nearest-neighbor sites and consumes the nutrient on that site.

- If $3/10 < R \leq 4/10$, the predatory reaction is selected. Then, if $R_1 < 1 - \exp(-p/V \times number\ of\ prey\ on\ the\ lattice \times number\ of\ predator\ on\ the\ lattice)$, the predatory reaction occurs. One of the predators on the lattice site generates another predator on one of the four nearest-neighbor sites and consumes the prey on that site.

- If $4/10 < R \leq 5/10$, predator death reaction is selected. Then, if $R_1 < 1 - \exp(-d_A \times number\ of\ predator\ on\ the\ lattice)$, the predator death reaction occurs. One of the predators on the lattice site dies.

- If $5/10 < R \leq 6/10$, prey death reaction is selected. Then, if $R_1 < 1 - \exp(-d_A \times number\ of\ prey\ on\ the\ lattice)$, the predator death reaction occurs. One of the prey on the lattice site dies.

- If $6/10 < R \leq 7/10$, mutation reaction is selected. Then, if $R_1 < 1 - \exp(-m \times number\ of\ prey\ on\ the\ lattice)$, the mutation reaction occurs. One of the prey on the lattice site dies, while a predator is generated on the same site.

- If $7/10 < R \leq 8/10$, predator competition reaction is selected. Then if $R_1 < 1 - \exp(-c_A/V \times number\ of\ predator\ on\ the\ lattice \times (number\ of\ predator\ on\ the\ lattice - 1))$, the predator competition reaction occurs. One of the predators on the lattice site dies.

- If $8/10 < R \leq 9/10$, prey competition reaction is selected. Then, if $R_1 < 1 - \exp(-c_B/V \times number\ of\ prey\ on\ the\ lattice \times (number\ of\ prey\ on\ the\ lattice - 1))$, the prey competition reaction occurs. One of the prey on the lattice site dies.

- If $9/10 < R \leq 1$, nutrient growth reaction is selected. Then, if $R_1 < 1 - \exp(-g)$, nutrient on the site increase by 1, unless $number\ of\ nutrient\ on\ the\ site = nutrient\ site\ capacity$.

- Once the procedures above have already been executed for all 20×3000 sites, we make all the nutrients hop one site forward and increase the time by one. Then we loop back to repeat the above procedure.

To continuously change the advection speed of the nutrient, we scale all the reaction rates by $1/U$ (e.g. $\tilde{p} = p/U$, $\tilde{g} = g/U$, etc.), and the simulation time by $1/U$. Parameter values used in the simulation are $D_A = D_B = 0.125$, $d_A = d_B = 0.02$, $p = 0.05$, $m = 0.0002$, $b = 0.05$, $c_A = c_B = 0.04$, $g = 20U^2/9$, site capacity of $N = 5$, and $c_N = 0.2$. The qualitative features of the phase diagram are not sensitive to small variations in these parameter values.

Simulation of our model is much faster than DNS of the Navier-Stokes equations, because only the large-scale features are mimicked.

III. SCALING OF NUTRIENT GROWTH RATE

The reason g has a quadratic dependence on U is based on an energy balance argument in pipe flow. Starting from the fluid at rest, the Navier-Stokes equation for the velocity $u(r,t)$ as a function of radial distance r in cylindrical geometry has a solution,

$$u(r,t) = -\frac{\partial_x p}{4\mu}(R^2 - r^2) + \frac{2(\partial_x p)R^2}{\mu} \sum_{n=1}^{\infty} \frac{1}{\lambda_x^3} \frac{J_0(\lambda_n r/R)}{J_1(\lambda_n)} e^{-\lambda_n^2 \frac{\nu t}{R^2}}, \tag{S.21}$$

where J_0 is the Bessel function of the first kind of order zero, λ_n are the positive roots of this function and $J_1(\lambda_n)$ is the Bessel function of the first kind of order one. In the expression in Eqn. (S.21), angular perturbation is ignored, and symmetry in the radial direction is assumed. These are good enough approximations in systems with high aspect ratio like the quasi-one-dimensional pipe flow studied in the present work.

From Eqn. (S.21), the growth rate of u is,

$$\partial_t u \sim \partial_x p, \tag{S.22}$$

while the recovery rate of laminar energy is proportional to $\partial_t u^2$. Since

$$u^2(r,t) = (\partial_x p)^2 \left[-\frac{1}{4\mu}(R^2 - r^2) + \frac{2R^2}{\mu} \sum_{n=1}^{\infty} \frac{1}{\lambda_x^3} \frac{J_0(\lambda_n r/R)}{J_1(\lambda_n)} e^{-\lambda_n^2 \frac{\nu t}{R^2}} \right]^2, \tag{S.23}$$

we get the scaling

$$\partial_t u^2 \sim (\partial_x p)^2. \tag{S.24}$$

Note that this is nothing but a result of dimensional analysis and symmetry argument. Since the pressure gradient along the x-direction is the driving force, and the rate of change in kinetic energy ($\propto \partial_t u^2$) should not depend on the direction of pressure gradient, it must scale as $(\partial_x p)^2$.

Since U in pipe flow satisfies,

$$\partial_x p \sim U, \tag{S.25}$$

the growth rate of the nutrient that represents the recovery rate of laminar solution scales as $g \sim U^2$.

---

[1] U. C. Täuber, Journal of Physics A: Mathematical and Theoretical **45**, 405002 (2012).